Engineering metal ion coordination to regulate amyloid fibril assembly and toxicity

Jijun Dong*, Jeffrey M. Canfield†, Anil K. Mehta*, Jacob E. Shokes‡, Bo Tian§, W. Seth Childers*, James A. Simmons*, Zixu Mao§, Robert A. Scott‡, Kurt Warncke*†, and David G. Lynn*¶

*Departments of Chemistry and Biology, Center for the Analysis of Supramolecular Self-Assemblies, and †Department of Physics, Emory University, Atlanta, GA 30322; ‡Department of Chemistry and Center for Metalloenzyme Studies, University of Georgia, Athens, GA 30602; and §Departments of Pharmacology and Neurology, Emory University School of Medicine, Atlanta, GA 30322

Edited by Harry B. Gray, California Institute of Technology, Pasadena, CA, and approved June 26, 2007 (received for review March 21, 2007)

Protein and peptide assembly into amyloid has been implicated in functions that range from beneficial epigenetic controls to pathological etiologies. However, the exact structures of the assemblies that regulate biological activity remain poorly defined. We have previously used Zn^{2+} to modulate the assembly kinetics and morphology of congeners of the amyloid β peptide (Aβ) associated with Alzheimer's disease. We now reveal a correlation among Aβ-Cu^{2+} coordination, peptide self-assembly, and neuronal viability. By using the central segment of Aβ, HHQKLVFFA or Aβ(13–21), which contains residues H13 and H14 implicated in Aβ-metal ion binding, we show that Cu^{2+} forms complexes with Aβ(13–21) and its K16A mutant and that the complexes, which do not self-assemble into fibrils, have structures similar to those found for the human prion protein, PrP. N-terminal acetylation and H14A substitution, Ac-Aβ(13–21)H14A, alters metal coordination, allowing Cu^{2+} to accelerate assembly into neurotoxic fibrils. These results establish that the N-terminal region of Aβ can access different metal-ion-coordination environments and that different complexes can lead to profound changes in Aβ self-assembly kinetics, morphology, and toxicity. Related metal-ion coordination may be critical to the etiology of other neurodegenerative diseases.

copper-binding | neurotoxicity | self-assembly

Protein intermolecular assembly, especially formation of amyloid fibrillar structures, is correlated with a variety of human neurodegenerative diseases, including Alzheimer's, Parkinson's, Huntington's, and Creutzfeldt–Jakob diseases (1). More recently, amyloid has been tied to many nonpathological functional roles. For example, formation and self-perpetuation of amyloids in *Saccharomyces cerevisiae* regulate diverse yeast phenotypic expression as a positive response to environmental fluctuations (2), and amyloid may be involved in long-term memory and synapse maintenance in the marine snail, Aplysia (3, 4). Many proteins, including archetypical globular proteins such as myoglobin, can also form amyloid fibrils, suggesting that amyloidogenesis may be an intrinsic property of any α-amino acid polymer (5). Accordingly, these highly ordered paracrystalline protein self-assemblies have now been recognized as useful for nanostructure fabrication and biotechnology (6–8). Fully capturing these technological opportunities and understanding the biological roles of amyloid will depend on further definition of the organized structure and assembly pathway.

Increasing evidence now implicates transition metal ions, including Zn^{2+}, Cu^{2+}, and Fe^{3+}, as contributors both to amyloid β (Aβ) assembly *in vitro* and to the neuropathology of Alzheimer's disease, AD (9). The obligatory region of metal ion (Zn^{2+}/Cu^{2+}) binding of Aβ has been mapped to the N terminus, amino acids 1–28 (10–16). In its soluble nonamyloid conformation, the peptide contains multiple intramolecular binding sites for Zn^{2+} and Cu^{2+} (9, 17), and intermolecular Zn^{2+} binding can promote Aβ aggregation (14, 18, 19). We have previously examined the role of these intermolecular Zn^{2+}-binding sites in the truncated peptide HHQALVFFA-NH_2, Aβ(13–21)K16A. This peptide contains the His-13/His-14 dyad previously implicated in metal binding (14, 15, 19) and the core hydrophobic sequence, LVFFA (20, 21) that is crucial for Aβ assembly. This short peptide self-assembles *in vitro* into typical amyloid fibrils that are morphologically similar to the full-length Aβ peptide (22). Zn^{2+} ions accelerate the assembly by means of coordination with two imidazole side chains from different peptide molecules. These two peptide molecules could be within a single β-sheet (intrasheet coordination), or come from adjacent sheets (intersheet coordination). Different metal coordination structures result in distinct self-assembled morphologies, ranging from typical amyloid fibrils to twisted ribbons and homogeneous nanotubes (22).

Complex coordination environments for Cu^{2+} appear to exist in the longer Aβ(1–40) peptide. An intermolecular His residue-bridging binding site of Cu^{2+} in the amyloid fibril (14), similar to Zn^{2+}-bridged His coordination (14, 18, 19, 22) has been indicated, whereas other results support an intramolecular Cu^{2+}–Aβ complex existing in both soluble and fibrillar Aβ(1–40) (23). As both inhibitory and fibril-inducing activities have been reported for Cu^{2+} (12, 24, 25), it is very likely that the observed differences in Cu^{2+} coordination might be directly responsible for the differences in kinetics and morphologies and, further, that these different Cu^{2+}–Aβ coordination structures can be accessed under slightly different experimental conditions. Indeed, Aβ(1–40) is capable of aggregating into a range of structures under slightly different assembly conditions (26). To simplify the study of Cu^{2+}-induced Aβ self-assembly, we prepared a series of homogeneous Aβ(13–21) complexes with both Zn^{2+} (22) and Cu^{2+} incorporation. The structural models that emerged from visible, infrared, x-ray absorption and electron paramagnetic resonance (EPR) spectroscopies reveal a molecular basis for the self-assembly characteristics of different Aβ(13–21) peptides. These models and initial neurotoxicity results implicate a critical role of metal ions and common structural features of amyloid assemblies in a range of neurological diseases.

Results and Discussion

Zn^{2+}/Cu^{2+} and the Assembly of Aβ(13–21)K16A. We considered Aβ(13–21), HHQKLVFFA, a minimum sequence for investi-

Author contributions: J.D., A.K.M., W.S.C., J.A.S., Z.M., R.A.S., K.W., and D.G.L. designed research; J.D., J.M.C., J.E.S., B.T., W.S.C., J.A.S., and K.W. performed research; J.D., J.M.C., A.K.M., J.E.S., B.T., W.S.C., J.A.S., Z.M., R.A.S., K.W., and D.G.L. analyzed data; and J.D., A.K.M., W.S.C., J.A.S., Z.M., K.W., and D.G.L. wrote the paper.

The authors declare no conflict of interest.

This article is a PNAS Direct Submission.

Abbreviations: Aβ(13–21)K16A, HHQALVFFA-NH_2; Ac-Aβ(13–21)H14A, CH_3CO-HAQKLVFFA-NH_2; ESEEM, electron spin echo envelope modulation; shfc, superhyperfine coupling.

¶To whom correspondence should be addressed. E-mail: david.lynn@emory.edu.

This article contains supporting information online at www.pnas.org/cgi/content/full/0702669104/DC1.

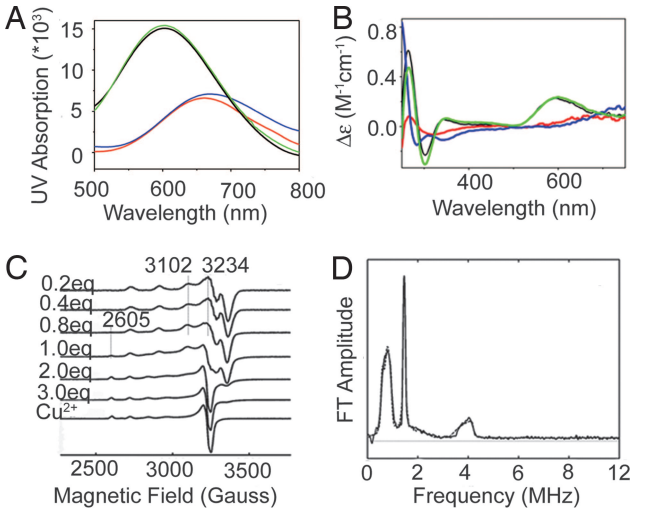

Fig. 1. Characterization of Cu^{2+}–Aβ(13–21) (HHQKLVFFA) congener complexes. (*A* and *B*) UV-Vis absorbance (*A*) and CD spectra (*B*) of 0.4 mM Cu^{2+} in the presence of 0.4 mM Aβ peptide. Black, Aβ(13–21)K16A; green, Aβ(Q15A); red, Aβ(H14A); and blue, Aβ(Ac-N). (*C*) CW-EPR spectra of the Cu^{2+}–Aβ(13–21)K16A complex with different Cu^{2+}-to-peptide ratios. The concentration of Aβ(13–21)K16A peptide is 0.5 mM. (*D*) Fourier transform (solid line) and simulation (dashed line) of three-pulse ESEEM for the soluble Cu^{2+}–Aβ(13–21)K16A complex prepared from 0.4 mM Cu^{2+} in the presence of 0.5 mM Aβ(13–21)K16A.

gating the role of metal-ion His binding in amyloid fibril formation because it contains the His-13/His-14 dyad previously implicated in metal binding (14, 15, 19) and a core hydrophobic sequence, LVFFA (20, 21), crucial for Aβ assembly. To isolate His-13/14 as the sole metal-binding site, Lys-16 was replaced with Ala, giving Aβ(13–21)K16A, which assembles into typical amyloid fibrils, following the characteristic conversion from random coil into β-strand (22). Zn^{2+} greatly accelerates the self-assembly rate and induces either typical amyloid fibrils or twisted ribbons and nanotubes depending on metal/peptide stoichiometry (22). These different morphologies arise from either intra- or intersheet His–Zn^{2+}–His complexation for the fiber and ribbons/nanotubes, respectively (22). In contrast, Cu^{2+} induces no CD β-signature in this peptide over extended time periods [see supporting information (SI) Fig. 6*A*], even in the presence of excess Zn^{2+} (data not shown), and no aggregates were pelleted when centrifuged at 16,110 × *g* for 30 min (SI Fig. 6*B*), supporting the lack of observable self-assembly. More strikingly, Cu^{2+} rapidly disaggregates amyloid fibrils preformed by Aβ(13–21)K16A (SI Fig. 6*C*) but was not able to dissociate peptide assemblies preformed in the presence of equimolar Zn^{2+} (data not shown).

Aβ(13–21)K16A Cu^{2+} Coordination. Inhibition of self-assembly in the presence of Cu^{2+} suggests that Cu^{2+} binds to the peptide. Isothermal titration calorimetry (ITC) measured the heat change upon Cu^{2+} binding and fit best to a one-site binding model, with each Cu^{2+} binding two Aβ(13–21)K16A molecules with an affinity constant (K_a) of 10^8 M (SI Fig. 7). Displacement of water from the $Cu^{2+}(H_2O)_6$ complex by a deprotonated amide nitrogen, amino group, imidazole nitrogen, carboxylate, and/or a water donor, causes a significant blue shift in λ_{max} (27) (see *SI Materials and Methods*). The Cu^{2+} transitions in the presence of one equivalent of Aβ(13–21)K16A in pH 5.6 buffer shifted to 600 nm ($\varepsilon \approx 40\ M^{-1}\ cm^{-1}$), which is characteristic of three- or four-nitrogen coordination in a type (II) square-planar or distorted tetragonal complex (Fig. 1*A*). The four bands present in the CD spectrum (Fig. 1*B*), are assigned as a 264-nm transition for a strong NH_2 and/or π_2 imidazole-to-Cu^{2+} charge transfer, 300 nm as charge transfer from N^- to Cu^{2+}, a weak 340-nm transition as charge transfer from π_1 imidazole to Cu^{2+}, and a 596-nm Cotton effect for a Cu^{2+} d–d transition (28). Virtually identical Cu^{2+} ITC, UV, and CD data were obtained for wild-type Aβ(13–21) (data not shown), suggesting that Cu^{2+} adopts the same coordination with both peptides.

The assignments were further tested with three fiber-forming single-point substitutions in Aβ(13–21)K16A: H14A, Q15A, and acetylation of the N-terminal amino group, Ac-N. Cu^{2+} bound and inhibited self-assembly of all three peptides (data not shown). Q15A retained the UV-Vis λ_{max} absorption at 600 nm ($\varepsilon \approx 40\ M^{-1}\ cm^{-1}$) (Fig. 1*A*) and a CD spectrum very similar to Aβ(13–21)K16A (Fig. 1*B*). These results argue against involvement of Gln-15 in Cu^{2+} binding. In contrast, both H14A and Ac-N exhibited red-shifted UV maxima and decreased absorption intensity (Fig. 1*A*) as well as dramatic changes in the CD spectra (Fig. 1*B*). These results (consistent with Eq. **5** in *SI Materials and Methods* and SI Table 1) implicate both His-14 and the N-terminal amine as coordinating ligands.

Cu^{2+} was interrogated directly with continuous wave—EPR (CW-EPR) after titration of Aβ(13–21)K16A with $CuCl_2$ (Fig. 1*C*). Identical line shapes were observed for samples with 0.2 and 0.4 molar equivalent (eq) of Cu^{2+}. At 0.8 eq, weak features characteristic of the aqueous copper complex, $Cu^{2+}(H_2O)_6$, emerged that broadened and distorted the line shape. At 1.0 eq Cu^{2+}, the $m_I = -3/2$ copper hyperfine feature of $Cu^{2+}(H_2O)_6$ at 2,605 G and the narrow derivative feature of $Cu^{2+}(H_2O)_6$ (peak, 3,200 G; trough, 3,250 G) appeared. The amplitude of the $Cu^{2+}(H_2O)_6$ spectrum becomes dominant over the Cu^{2+}–Aβ(13–21)K16A spectrum with 2 and 3 eq of Cu^{2+}. These results are consistent with ITC confirming a stoichiometry of 0.5 eq of Cu^{2+} per peptide. The EPR spectrum with 0.4 eq of Cu^{2+} (Fig. 1*C*) best represents the line shape of the Cu^{2+}–peptide complex and is characterized by $g_{\|} = 2.236$, and a copper hyperfine splitting at $a_{\|}$ of 196 G, consistent with coordination by 2N2O or 3N1O or 4N equatorial ligands (29) (summarized in SI Table 1).

The three-pulse electron spin echo envelope modulation (ESEEM) spectrum of the Aβ(13–21)K16A complex with Cu^{2+} (Fig. 1*D*) is characteristic of superhyperfine coupling (shfc) between the electron on Cu^{2+} and a ^{14}N nucleus, where the shfc and nuclear Zeeman contributions approximately cancel for one electron spin manifold ($A/2 \approx \nu_N$, where A is the shfc constant and ν_N is the ^{14}N free nuclear frequency) (30, 31). This "exact cancellation" condition gives rise to the sharp lines at 0.6, 0.8, and 1.4 MHz in the ESEEM spectrum, which are assigned to the ν_0, ν_- and ν_+ ^{14}N nuclear quadrupole transitions, respectively (32). The broad feature at 4 MHz arises from the $\Delta m_I = \pm 2$ splitting in the electron spin manifold where the shfc and nuclear Zeeman contributions are additive. The pattern in the ESEEM spectrum (Fig. 1*D*) and the simulation values (SI Table 2) are characteristic of imidazole coordination to Cu^{2+}, and arise from the uncoordinated, remote nitrogen of imidazole (30, 31, 33). These results establish that one histidine imidazole coordinates Cu^{2+} in an equatorial position.

Therefore, ITC established that Cu^{2+} binds two Aβ(13–21)K16A peptides. The CD blue shifted d–d transition and ellipticity at 596 nm strongly support Cu^{2+} coordination to a deprotonated amide nitrogen (11, 34–36). Cu^{2+} is known to chelate backbone amides, particularly if available histidine residues or an α amino group provide an anchor point for the metal ion (37). In these cases, Cu^{2+} can promote peptide nitrogen ionization at pH values as low as 5–6, even though the pK_a is 12–13 in solution. The value of $\Delta\varepsilon/n$ for the charge transfer between N^- and Cu^{2+} at 300 nm is fairly constant, in the range of 0.2–0.3, where n is the number of negatively charged peptide nitrogens involved in coordination (28). Therefore, $\Delta\varepsilon$ (300 nm) ≈ 0.23 (Fig. 1*B*) indicates Cu^{2+} coordination with one

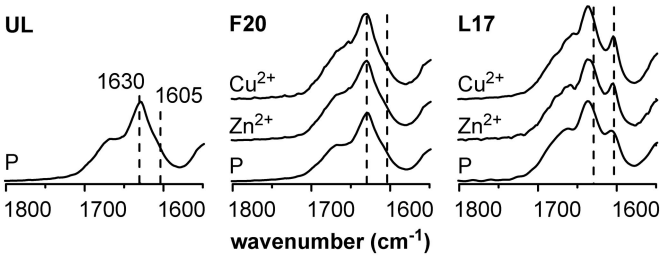

Fig. 2. Isotope edited FT-IR. Absorption of amide I bands of Ac-Aβ(13–21)H14A (Ac-HAQKLVFFA) fibrils formed with free peptide (P) and in the presence of Zn^{2+} or Cu^{2+}. UL, unlabeled peptide; F20, $^{13}C{=}O$ was introduced into the peptide at Phe-20; L17, $^{13}C{=}O$ was introduced into the peptide at Leu-17.

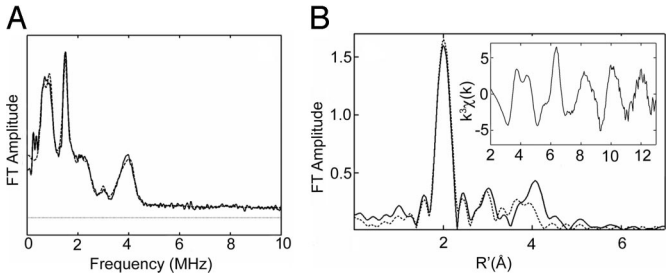

Fig. 3. Copper ion analysis in the Ac-Aβ(13–21)H14A (Ac-HAQKLVFFA) fibrillar complex. (*A*) Fourier transform (solid line) and simulation (dashed line) of three-pulse ESEEM for Cu^{2+}-Ac-Aβ(13–21)H14A fibrils. Simulation values are summarized in SI Table 2. (*B*) The Fourier transform of extended x-ray absorption fine-structure (EXAFS) (*Inset*) of Cu^{2+}-Ac-Aβ(13–21)H14A fibrils. Solid line, experiment; dashed line, fit 8 (values listed in SI Table 4).

deprotonated backbone amide. Coordination to the N-terminal amine, the amide backbone, and one equatorial histidine residue requires His-13 and His-14 to form a tridentate metal complex, making structure **1** (SI Fig. 8) the most energetically accessible structure. The asymmetric α-carbon of His-14, held in the chelating ring between a main-chain amide nitrogen and a histidine imidazole ring, provides a vicinal effect (38, 39), consistent with the intense CD signal at 596 nm for the Cu^{2+} d–d transition. Finally, the conclusion from ITC that Cu^{2+} binds with two Aβ(13–21)K16A peptides indicates that the open coordination site is occupied by a ligand from the second peptide.

Design of Ac-Aβ(13–21)H14A for Cu^{2+}-Induced Self-Assembly. In contrast to Zn^{2+} (22), Cu^{2+} inhibits assembly of Aβ(13–21)K16A by deprotonating a backbone amide nitrogen and rearranging the peptide backbone to create a chelated metal complex. Even when the amino group is acetylated, as in Aβ(Ac-N), which results in loss of the amide nitrogen as a ligand, as suggested by the disappearance of the CD absorption at 600 nm (Fig. 1*B* and SI Table 1), amyloid fibril formation remains inhibited. In this case, Cu^{2+} appears to bind with both His-13 and His-14 intramolecularly, preventing extended β-strand formation and self-assembly (SI Table 1). Therefore, we designed a peptide Ac-Aβ(13–21)H14A, CH_3CO-HAQKLVFFA-NH_2, where removal of both His-14 and the free amino group would limit the ligands accessible to Cu^{2+} in each peptide molecule to a single His-13.

During incubation at pH 7.0, Ac-Aβ(13–21)H14A developed the characteristic β-sheet signature seen with Aβ(13–21)K16A and other Aβ peptides (SI Fig. 9*A*) (22). In the presence of one equivalent of Zn^{2+} or Cu^{2+}, the β-signature developed more rapidly (SI Fig. 8*B*). Concurrent with the CD-detected transition in all three samples, the initial FT-IR amide I random coil stretch at $\approx$1,645 cm^{-1} was replaced by a β-sheet stretch at 1,630 cm^{-1} both in the absence and presence of metal ions (data not shown) (40). Although the absent or present metal-ion fibrils displayed similar structure, their morphology differed. In the absence of metal ions, typical amyloid fibrils and tightly twisted fibers were apparent by atomic force microscopy (SI Fig. 9*C*) and transmission electron microscopy (TEM, data not shown) with diameters of 8 nm. The fibrils formed in the presence of Zn^{2+} or Cu^{2+} were both nontwisted and smooth, with diameters of 8–9 nm (SI Fig. 9 *D* and *E*).

Structural Characterization of Metal Ion-Induced Amyloid Fibrils. Isotope-edited FT-IR (Fig. 2) was used to probe the local structures of the metal-free and metal-induced amyloid fibrils (41–45). In Ac-Aβ(13–21)H14A, $^{13}C{=}O$ labels were placed in the middle of the sequence, [1-^{13}C]L17, or close to the C terminus, [1-^{13}C]F20. In metal-free amyloid fibrils, the [1-^{13}C]F20 amide stretch has an extremely weak shoulder at 1,605 cm^{-1}. The [1-^{13}C]L17 peptide also has a band at 1,605 cm^{-1}, but with increased intensity, and an absorption maximum shift from 1,630 to 1,637 cm^{-1} for $^{12}C{=}O$. This shift results from disturbance of the ^{12}C hydrogen-bonding network by ^{13}C (46) and is not observed for [1-^{13}C]F20-labeled fibrils. The stronger intensity for the [1-^{13}C]L17 carbonyl carbon is consistent with Leu-17 being buried in the fibril hydrophobic core with more ordered hydrogen bonding. The isotope-edited IR spectra of fibrils formed in the absence and presence of Zn^{2+} or Cu^{2+} ions are identical in both labeling schemes. This result further confirms a very similar, if not identical, peptide conformation and packing order within the fibril β-sheets.

Extent of Metalation of the Ac-Aβ(13–21)H14A Fibrils. ITC cannot deconvolute metal binding from peptide–peptide association during Ac-Aβ(13–21)H14A amyloid assembly. Therefore, amino acid analysis (AAA) and inductively coupled plasma mass spectrometry (ICP-MS) were performed to determine the metal-to-peptide ratio in the metalated Ac-Aβ(13–21)H14A fibrils (SI Table 3). Initial peptide concentration was 2 mM, with differing initial metal concentrations ranging from 0.5 to 2 mM. After maturation, fibers were pelleted, washed, and subjected to AAA and ICP-MS measurements. The Zn^{2+}-to-peptide ratio varied from 0.48 to 0.64, and the Cu^{2+}-to-peptide ratio varied from 0.55 to 0.73. The imprecision in incorporation ratios probably arises from nonspecifically bound metal ions. The results establish a peptide-to-metal ratio close to 2:1 in both the Zn^{2+} and Cu^{2+} assemblies.

Coordination Environment of Metal Ions in Ac-Aβ(13–21)H14A Fibrils. To specifically characterize the Cu^{2+} coordination responsible for induction of amyloid fibrils, Cu^{2+}–fibrillar complexes were pelleted, rinsed, and resuspended in fresh buffer. The three-pulse ESEEM spectrum of the Cu^{2+}–fibrillar complex (Fig. 3*A*) shows ν_0, ν_-, and ν_+ nuclear quadrupole features at the same frequency positions, 0.6, 0.8, and 1.4 MHz, as observed for the Cu^{2+}–Aβ(13–21)K16A complex (Fig. 1*D*). In addition, weaker peaks are present that correspond to combinations of the fundamental frequencies, including bands centered at 2.1 MHz ($[\nu_0+\nu_+]$ and $[\nu_- + \nu_+]$) and at 2.8 MHz ($[\nu_+ + \nu_+]$). Combination lines in ESEEM spectra indicate the presence of multiple nuclear couplings, and the relative amplitudes of the fundamental and combination features (47) are consistent with two coupled ^{14}N nuclei, with e^2qQ/h = 1.55 MHz and η = 0.751 (SI Table 2). The simulation parameters and spectral pattern, including the enhanced amplitude of the $\Delta m_I = \pm 2$ feature at 4 MHz, demonstrate coupling of Cu^{2+} to two remote ^{14}N atoms of distinct histidine imidazoles, establishing that two histidine imidazoles are coordinated equatorially to Cu^{2+} in the fibrillar complex.

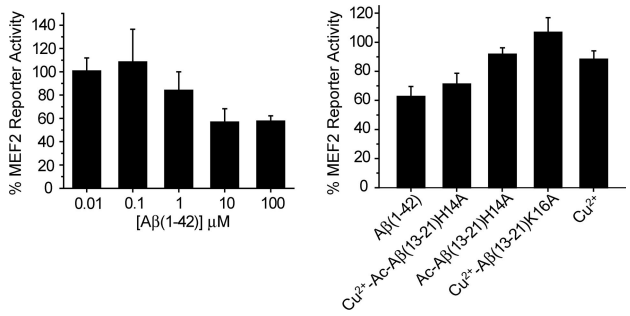

Fig. 4. MEF2 luciferase reporter gene assay. (*Left*) Aβ(1–42) dose-dependent response. (*Right*) Cu^{2+}–Ac-Aβ(13–21)H14A fibrils are as toxic as Aβ(1–42) and Aβ(10–35) fibrils and Cu^{2+}–Aβ(13–21)K16A complex is nontoxic. Peptide concentration is 10 μM.

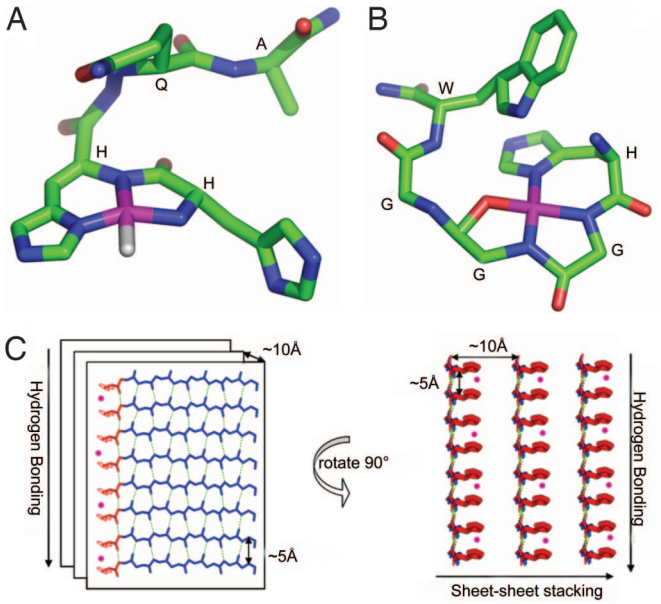

Fig. 5. Structural models for the Cu^{2+}–peptide complexes. (*A*) Proposed model for Cu^{2+} coordination with Aβ(13–21)K16A showing only the first four residues (HHQA). (*B*) Crystal structure for Cu^{2+}–HGGGW complex, the N-terminal repeat sequence of human prion protein (63). Only equatorial ligands are illustrated in both models. Purple, Cu ion; green, carbon; red, oxygen; blue, nitrogen; gray, unidentified ligand. (*C*) Structural models for Cu^{2+} arrangement in Ac-Aβ(13–21)H14A fibrils. (*Left*) View of three stacked β-sheets. (*Right*) View down peptide backbone. H-bonds are parallel to fibril long axis, and fibrils consist of parallel in-register β-sheets in both the absence and presence of metal ions. Sheets stack perpendicular to the H-bond direction. Both Zn^{2+} and Cu^{2+} coordinate two histidines along the H-bonding dimension within the same β-sheet. Red, His-13; blue, remaining Ac-Aβ(13–21)H14A residues; magenta, Zn^{2+}, Cu^{2+}; and green, H-bonds between backbone carbonyl and amide. Amino acid side chains, except His-13, are removed for clarity.

Following previously developed procedures for probing Zn^{2+} coordination environments (22), Ac-Aβ(13–21)H14A fibrils were characterized by extended x-ray absorption fine structure (EXAFS) spectroscopy. Curve fitting indicates 3N/1O or 2N/2O or 1N/3O atoms in the first shell (SI Table 4). The coincident appearance and intensities of the 3-Å and 4-Å peaks in the Fourier transform EXAFS spectra [Fig. 3*B* for Cu^{2+} and ref. 22 for Zn^{2+} Ac-Aβ(13–21)H14A fibrillar complexes] are diagnostic of two imidazole ligands. The best fit (dashed line in Fig. 3*B*) was generated by using two His imidazoles and two additional first-shell light atoms (N or O) (SI Table 4, Fit 8). Therefore, both Zn^{2+} and Cu^{2+} induce Ac-Aβ(13–21)H14A fibril formation by bridging two His-13 residues between parallel hydrogen-bonded β-strands in a His–metal^{2+}–His chelated structure.

Toxicity of Cu^{2+}–Peptide Complexes. Initial neurotoxicity assays in cultured neurons suggested that the two Cu^{2+}–peptide coordination environments [Cu^{2+}–Aβ(13–21)K16A complex and Cu^{2+}–Ac-Aβ(13–21)H14A fibrils] were biologically distinct (data not shown). To more specifically characterize the activity, a myocyte enhancer factor 2 (MEF2) assay was developed in SN4741, a dopaminergic neuron cell line derived from the mouse midbrain. The MEF2 family of transcription factors play critical roles in diverse cellular processes including neuronal survival (48). MEF2s are an endpoint for several neurotoxic signaling pathways that control the molecular machinery of cellular apoptosis (49, 50). As shown in Fig. 4 *Left*, Aβ(1–42) regulates MEF2. In addition, inhibition of MEF2 activity by mature peptide assemblies is dose-dependent and peptide-specific. The Cu^{2+}–Ac-Aβ(13–21)H14A fibrils are equally as inhibitory as Aβ(1–42), whereas the Cu^{2+}-free Ac-Aβ(13–21)H14A fibrils and Cu^{2+} ions alone are ineffective. The soluble Cu^{2+}–Aβ(13–21)K16A complex is also nontoxic, suggesting that different Cu^{2+} chelation environments, as mediated by different Aβ conformations, compromise neuron viability.

Summary. Metal ion association with Aβ has frequently been correlated with Alzheimer's disease (11, 35, 51, 52), and the link among metal-coordination structure, the impact on assembly kinetics, and overall aggregation remains critical to understanding disease etiology. Our attempts to identify individual metal sites within Aβ segments now reveal that Cu^{2+} coordination can radically alter assembly kinetics and morphology. In the short Aβ fragment Aβ(13–21)K16A, backbone deprotonation occurs even at low pH to generate a high affinity ($K_a = 10^8$ M) Cu^{2+}-binding site. The five- {NH_2, N^-_{amide}} and six-membered {N^-_{amide}, N_{Im}} metal chelate in structure **1** (SI Fig. 8) coordinates with a second peptide, probably through a histidine residue. A virtually identical {NH_2, N^-_{amide}, N_{Im}} complex was previously observed for several short peptides that contain His as the second residue from the peptide N terminus, such as X-His (X = Ala, Gly, His) or X-His-Y (X = Ala, Gly, and Y = Ala, Leu, Lys) (53–56). In Aβ(13–21)K16A, this X-His (X = His) motif retards β-strand and β-sheet assembly, but this inhibition may be unique to Cu^{2+} because Zn^{2+} readily promotes amyloid self-assembly (22). Even with acetylation of the N terminus as in Ac-Aβ(13–21)K16A, Cu^{2+} coordinates with both His-13 and His-14 intramolecularly to retard peptide assembly. This inhibition of assembly was previously observed for Ac-Aβ(11-X) (X = 16, 20, 28) (57, 58), probably through a similar complex.

Removing one histidine, as in Ac-Aβ(13–21)H14A, generates a peptide in which both Zn^{2+} and Cu^{2+} accelerate amyloid fibril formation by capturing intermolecular His–metal–His coordination (Fig. 5*C*). The isotope-edited FT-IR results predict a parallel, in-register β-sheet organization, an assignment further supported by preliminary solid-state NMR results (data not shown). The same conformation was previously determined for the well characterized Aβ(10–35) peptide assembled in the absence of metal ions (21, 59). Here, both Zn^{2+} and Cu^{2+} associate with two His-13 residues from adjacent peptides arranged along the growing β-sheet surface (22), increasing the growth rate and stability of the growing fibril. Stoichiometry analyses are consistent with the organized linear array of metal ions along the fibril surface (Fig. 5*C*). Therefore, the ability of Cu^{2+} to access the intermolecular coordination environment depends on subtle changes in the intramolecular site for Cu^{2+}.

In this regard, Aβ(1–40) is certainly capable of aggregating into a variety of structures under slightly different assembly conditions (26), and metals clearly contribute to this shifting

morphological landscape. In contrast to the short peptides, as more residues are involved in fibril β-sheet formation of full-length Aβ, the forces associated with peptide self-assembly may well dictate fibril morphology, overwhelming the contribution of metal-mediated assembly. For example, the first 10 residues of Aβ(1–40) are not included in the core β-sheet of the fibrils but, rather, are structurally disordered and exposed along the fibril surface (60). Intramolecular metal complexation close to this structurally flexible region may slow assembly (24), but, as observed in these short peptides, does not block assembly.

"Switching" to achieve different Cu^{2+}-binding sites and peptide conformations has also been considered for the mammalian prion protein (PrP). Cu^{2+} binds primarily to the N terminus of PrP, a region that is structurally flexible and outside of the core assembly region (61). Therefore, metal-binding regions in both Aβ and PrP are in the structurally flexible N-terminal domain and lie outside the amyloid-determining core (21, 62). The N terminus of PrP contains four copies of the Cu^{2+}-binding octarepeat sequence, PHGGGWGQ. In the presence of two or more molar equivalents of Cu^{2+}, the metal ions bind in an intrarepeat manner, with ligands supplied by one histidine imidazole, two deprotonated amides from the next two glycines, and the amide carbonyl of the second glycine (63) (Fig. 5*B*). At low Cu^{2+} concentrations or under acidic pH conditions, multiple His imidazoles from different octarepeats coordinate with Cu^{2+}, forming interrepeat binding sites (64, 65). These interrepeat sites could be intramolecular, intermolecular, or a combination (65).

Moreover, several proteins associated with neurodegenerative diseases also bind metal ions, and metal binding modulates the aggregation behavior of these proteins. α-Synuclein (α-Syn), a protein associated with Parkinson's disease (PD), is intrinsically unfolded and Cu^{2+} binding results in rapid aggregation (66). Superoxide dismutase 1 (SOD1), a CuZn metalloprotein that catalyzes the dismutation of the superoxide anion, is associated with the progressive neurodegenerative disease amyotrophic lateral sclerosis (ALS). Cu^{2+} and Zn^{2+} bind and organize a loop region of SOD1, and mutations around the binding site that result in alterations of the coordination environment of Cu^{2+} and Zn^{2+} lead to misfolding and aggregation of SOD1 (67, 68). The oxidative modification and aggregation of SOD1 has been correlated with both AD and PD (69). Thus, it seems reasonable to speculate that AD, PD, and ALS share common mechanisms of metal ion regulation and/or metal-ion induction of protein aggregation, which might lead to a common, or at least overlapping, pathogenic mechanism(s).

Our studies now establish that the N-terminal region of Aβ can access a range of metal-coordination structures. These results suggest that the effect of metal ions in neurodegenerative diseases is not simply a result of metal ion on/off binding, but is due to switching between different metal-binding modes. Clearly, the short peptides allow these structures to be constructed and evaluated directly, whereas in the larger Aβ peptides, the accessible conformations and subtle environmental conditions can alter ligand accessibility and modulate both amyloid assembly and cellular toxicity. The striking quasilinear array of Cu^{2+} ions along the surface of the biologically active Ac-Aβ(13–21)H14A fibril suggests that assembly within a complex cellular milieu will certainly produce novel protein architectures, architectures that can now be constructed and evaluated directly for functional neuron toxicity and prion function.

Materials and Methods

Fibril Formation. Each Aβ(13–21) congener peptide was dissolved completely in distilled deionized H_2O, sonicated for 10 min, and centrifuged at 16,110 $\times$ *g* for 10 min. The supernatant was used as stock solution for each peptide. Samples with desired peptide and metal concentration in 25 mM Mes buffer (pH 5.6) or Hepes buffer (pH 7.2) and 10 mM NaCl were prepared from stock solutions.

Spectroscopy. UV-Vis absorption spectra were obtained on a V-530 UV/VIS spectrometer (Jasco, Easton, MD) with a 1-cm path-length quartz cuvette. CD spectra were recorded on a Jasco 810 CD spectropolarimeter. Ellipticity (θ, m degrees) was converted to mean residue molar ellipticity (MRME) $[\theta] = \theta/(10 \times n \times C \times l)$ or to molar ellipticity $\Delta\varepsilon = \theta/(32980 \times C \times l)$, where n is number of amide bonds per peptide, C is molar concentration (mol/liter), and l is path length (cm). FT-IR spectra were collected on a Magna 560 IR spectrometer (Nicolet, Madison, WI). Mature fibrils were spun down, lyophilized, mixed, and ground with KBr and pressed into transparent disks. Typically, 100 scans were averaged with 4-cm^{-1} resolution. X-ray absorption spectra were collected at the Stanford Synchrotron Radiation Laboratory on beamline 9-3. Mature fibrils were spun down and washed with fresh buffer solution three times. The hydrated pellet was transferred to a 25-well sample holder, frozen, and stored in liquid nitrogen until data collection. See *SI Materials and Methods* for instrumental setup and data analysis.

EPR. Samples for both EPR and ESEEM were mixed with an equal volume of ethylene glycol, transferred to 4 mm o.d. quartz EPR tubes, frozen in liquid nitrogen-chilled 2-methylbutane ($\approx$150 K), and stored in liquid nitrogen. Continuous-wave EPR spectra were collected on a ER200D EPR spectrometer (Bruker, Billerica, MA). ESEEM spectra were collected on a home-built pulsed-EPR spectrometer by using the three-pulse stimulated echo pulse sequence. Details of EPR and ESEEM experiments and simulations (70, 71) are described in *SI Materials and Methods*.

Microscopy. AFM samples were placed on silicon chips and imaged under dry conditions in tapping mode on a JSPM-4210 AFM (JEOL, Tokyo, Japan) by using ultrasharp noncontact silicon cantilevers with typical frequencies from 240 to 350 kHz.

MEF2 Assay. SN4741 cells were transiently transfected with a DNA construct containing a luciferase gene under control of MEF2 enhancer by using the Lipofectamine 2000 transfection system (Invitrogen, Carlsbad, CA). Total transfected DNA was kept constant. After 24 h of transfection, cells were treated with Aβ peptides that had been assembled as described above. Twenty-four hours after Aβ treatment, cell lysates were analyzed for luciferase activity by using Luciferase reporter gene assay kit (Roche, Mannheim, Germany).

We thank James Lah and Craig Heilman for initial neurotoxicity assays, Yi Xu and Rong Ni for assistance with peptide synthesis and purifications, and C. L. Emerson for AFM instrumentation. This work was supported by Department of Energy (DOE) Grant ER15377 (to D.G.L.), National Institutes of Health (NIH) National Institute of General Medical Sciences Grant GM42025 (to R.A.S.), NIH Grants AG 023695 and NS 048254 and the R. W. Woodruff Health Sciences Center Fund (to Z.M.), Emory Alzheimer's Disease Center Grant P50 AG025688 (to D.G.L. and Z.M.), and National Science Foundation Grant CHE-0131013 (for CD instrumentation). The Stanford Synchrotron Radiation Laboratory is a national user facility operated by Stanford University (Stanford, CA) on behalf of the U.S. DOE, Office of Basic Energy Sciences. The SSRL Structural Molecular Biology Program is supported by DOE, Office of Biological and Environmental Research and by the NIH National Center for Research Resources and Biomedical Technology Program. AAA analysis was performed by the Keck Biotechnology Resource Laboratory at Yale University (New Haven, CT), and ICP-MS was performed at the Chemical Analysis Laboratory at the University of Georgia.

1. Carrell RW, Lomas DA (1997) *Lancet* 350:134–138.
2. Patino MM, Liu JJ, Glover JR, Lindquist S (1996) *Science* 273:622–626.
3. Si K, Giustetto M, Etkin A, Hsu R, Janisiewicz AM, Miniaci MC, Kim JH, Zhu H, Kandel ER (2003) *Cell* 115:893–904.
4. Si K, Lindquist S, Kandel ER (2003) *Cell* 115:879–891.
5. Dobson CM (2003) *Nature* 426:884–890.
6. Scheibel T, Parthasarathy R, Sawicki G, Lin XM, Jaeger H, Lindquist SL (2003) *Proc Natl Acad Sci USA* 100:4527–4532.
7. Reches M, Gazit E (2003) *Science* 300:625–627.
8. Silva GA, Czeisler C, Niece KL, Beniash E, Harrington DA, Kessler JA, Stupp SI (2004) *Science* 303:1352–1355.
9. Bush AI, Pettingell WH, Multhaup G, Paradis MD, Vonsattel JP, Gusella JF, Beyreuther K, Masters CL, Tanzi RE (1994) *Science* 265:1464–1467.
10. Bush AI, Multhaup G, Moir RD, Williamson TG, Small DH, Rumble B, Pollwein P, Beyreuther K, Masters CL (1993) *J Biol Chem* 268:16109–16112.
11. Syme CD, Nadal RC, Rigby SE, Viles JH (2004) *J Biol Chem* 279:18169–18177.
12. Atwood CS, Moir RD, Huang XD, Scarpa RC, Bacarra NME, Romano DM, Hartshorn MK, Tanzi RE, Bush AI (1998) *J Biol Chem* 273:12817–12826.
13. Curtain CC, Ali F, Volitakis I, Cherny RA, Norton RS, Beyreuther K, Barrow CJ, Masters CL, Bush AI, Barnham KJ (2001) *J Biol Chem* 276:20466–20473.
14. Miura T, Suzuki K, Kohata N, Takeuchi H (2000) *Biochemistry* 39:7024–7031.
15. Liu ST, Howlett G, Barrow CJ (1999) *Biochemistry* 38:9373–9378.
16. Yang DS, McLaurin J, Qin K, Westaway D, Fraser PE (2000) *Eur J Biochem* 267:6692–6698.
17. Atwood CS, Scarpa RC, Huang XD, Moir RD, Jones WD, Fairlie DP, Tanzi RE, Bush AI (2000) *J Neurochem* 75:1219–1233.
18. Stellato F, Menestrina G, Dalla Serra M, Potrich C, Tomazzolli R, Meyer-Klaucke W, Morante S (2006) *Eur Biophys J* 35:340–351.
19. Morgan DM, Dong J, Jacob J, Lu K, Apkarian RP, Thiyagarajan P, Lynn DG (2002) *J Am Chem Soc* 124:12644–12645.
20. Lu K, Jacob J, Thiyagarajan P, Conticello VP, Lynn DG (2003) *J Am Chem Soc* 125:6391–6393.
21. Benzinger TLS, Gregory DM, Burkoth TS, Miller-Auer H, Lynn DG, Botto RE, Meredith SC (1998) *Proc Natl Acad Sci USA* 95:13407–13412.
22. Dong J, Shokes JE, Scott RA, Lynn DG (2006) *J Am Chem Soc* 128:3540–3542.
23. Karr JW, Kaupp LJ, Szalai VA (2004) *J Am Chem Soc* 126:13534–13538.
24. Zou J, Kajita K, Sugimoto N (2001) *Angew Chem Int Ed Engl* 40:2274–2277.
25. Suzuki K, Miura T, Takeuchi H (2001) *Biochem Biophys Res Commun* 285:991–996.
26. Petkova AT, Leapman RD, Guo Z, Yau WM, Mattson MP, Tycko R (2005) *Science* 307:262–265.
27. Sigel H, Martin RB (1982) *Chem Rev* 82:385–426.
28. Daniele PG, Prenesti E, Ostacoli G (1996) *J Chem Soc Dalton* 3269–3275.
29. Peisach J, Blumberg WE (1974) *Arch Biochem Biophys* 165:691–708.
30. Mims WB, Peisach J (1978) *J Chem Phys* 69:4921–4930.
31. Flanagan HL, Singel DJ (1987) *J Chem Phys* 87:5606–5616.
32. Lucken EAC (1969) *Nuclear Quadrupole Coupling Constants* (Academic, London).
33. Jiang F, McCracken J, Peisach J (1990) *J Am Chem Soc* 112:9035–9044.
34. Stanczak P, Valensin D, Juszczyk P, Grzonka Z, Migliorini C, Molteni E, Valensin G, Gaggelli E, Kozlowski H (2005) *Biochemistry* 44:12940–12954.
35. Kowalik-Jankowska T, Ruta M, Wisniewska K, Lankiewicz L (2003) *J Inorg Biochem* 95:270–282.
36. Brown DR, Guantieri V, Grasso G, Impellizzeri G, Pappalardo G, Rizzarelli E (2004) *J Inorg Biochem* 98:133–143.
37. Sundberg RJ, Martin RB (1974) *Chem Rev* 74:471–517.
38. Nakanishi K, Nina E, Woody RW (1994) *Circular Dichroism: Principles and Applications* (Wiley–VCH, New York), p 223.
39. Tsangaris JM, Martin RB (1970) *J Am Chem Soc* 92:4255–4260.
40. Fabian H, Szendrei GI, Mantsch HH, Otvos L, Jr (1993) *Biochem Biophys Res Commun* 191:232–239.
41. Lu K (2005) PhD dissertation (Emory Univ, Atlanta).
42. Paul C, Axelsen PH (2005) *J Am Chem Soc* 127:5754–5755.
43. Hiramatsu H, Goto Y, Naiki H, Kitagawa T (2005) *J Am Chem Soc* 127:7988–7989.
44. Lansbury PT, Jr, Costa PR, Griffiths JM, Simon EJ, Auger M, Halverson KJ, Kocisko DA, Hendsch ZS, Ashburn TT, Spencer RG, *et al.* (1995) *Nat Struct Biol* 2:990–998.
45. Silva RA, Barber-Armstrong W, Decatur SM (2003) *J Am Chem Soc* 125:13674–13675.
46. Brauner JW, Dugan C, Mendelsohn R (2000) *J Am Chem Soc* 122:677–683.
47. McCracken J, Pember S, Benkovic SJ, Villafranca JJ, Miller RJ, Peisach J (1988) *J Am Chem Soc* 110:1069–1074.
48. Mao Z, Bonni A, Xia F, Nadal-Vicens M, Greenberg ME (1999) *Science* 286:785–790.
49. Gong X, Tang X, Wiedmann M, Wang X, Peng J, Zheng D, Blair LA, Marshall J, Mao Z (2003) *Neuron* 38:33–46.
50. Tang X, Wang X, Gong X, Tong M, Park D, Xia Z, Mao Z (2005) *J Neurosci* 25:4823–4834.
51. Karr JW, Akintoye H, Kaupp LJ, Szalai VA (2005) *Biochemistry* 44:5478–5487.
52. Kozin SA, Zirah S, Rebuffat S, Hoa GH, Debey P (2001) *Biochem Biophys Res Commun* 285:959–964.
53. Kozlowski H, Bal W, Dyba M, Kowalik-Jankowska T (1999) 184:319–346.
54. Bruni S, Cariati F, Daniele PG, Prenesti E (2000) *Spectrochim Acta A* 56:815–827.
55. Conato C, Gavioli R, Guerrini R, Kozlowski H, Mlynarz P, Pasti C, Pulidori F, Remelli M (2001) *Biochim Biophys Acta* 1526:199–210.
56. Livera CE, Pettit LD, Bataille M, Perly B, Kozlowski H, Radomska B (1987) *J Chem Soc Dalton* 661–666.
57. Kowalik-Jankowska T, Ruta-Dolejsz M, Wisniewska K, Lankiewicz L, Kozlowski H (2000) *J Chem Soc Dalton* 4511–4519.
58. Kowalik-Jankowska T, Ruta-Dolejsz M, Wisniewska K, Lankiewicz L (2002) *J Inorg Biochem* 92:1–10.
59. Burkoth TS, Benzinger TLS, Urban V, Morgan DM, Gregory DM, Thiyagarajan P, Botto RE, Meredith SC, Lynn DG (2000) *J Am Chem Soc* 122:7883–7889.
60. Petkova AT, Ishii Y, Balbach JJ, Antzutkin ON, Leapman RD, Delaglio F, Tycko R (2002) *Proc Natl Acad Sci USA* 99:16742–16747.
61. Donne DG, Viles JH, Groth D, Mehlhorn I, James TL, Cohen FE, Prusiner SB, Wright PE, Dyson HJ (1997) *Proc Natl Acad Sci USA* 94:13452–13457.
62. James TL, Liu H, Ulyanov NB, Farr-Jones S, Zhang H, Donne DG, Kaneko K, Groth D, Mehlhorn I, Prusiner SB, *et al.* (1997) *Proc Natl Acad Sci USA* 94:10086–10091.
63. Millhauser GL (2004) *Acc Chem Res* 37:79–85.
64. Chattopadhyay M, Walter ED, Newell DJ, Jackson PJ, Aronoff-Spencer E, Peisach J, Gerfen GJ, Bennett B, Antholine WE, Millhauser GL (2005) *J Am Chem Soc* 127:12647–12656.
65. Morante S, Gonzalez-Iglesias R, Potrich C, Meneghini C, Meyer-Klaucke W, Menestrina G, Gasset M (2004) *J Biol Chem* 279:11753–11759.
66. Rasia RM, Bertoncini CW, Marsh D, Hoyer W, Cherny D, Zweckstetter M, Griesinger C, Jovin TM, Fernandez CO (2005) *Proc Natl Acad Sci USA* 102:4294–4299.
67. Antonyuk S, Elam JS, Hough MA, Strange RW, Doucette PA, Rodriguez JA, Hayward LJ, Valentine JS, Hart PJ, Hasnain SS (2005) *Protein Sci* 14:1201–1213.
68. Valentine JS, Hart PJ (2003) *Proc Natl Acad Sci USA* 100:3617–3622.
69. Choi J, Rees HD, Weintraub ST, Levey AI, Chin LS, Li L (2005) *J Biol Chem* 280:11648–11655.
70. Canfield JM, Warncke K (2002) *J Phys Chem B* 106:8831–8841.
71. Canfield JM, Warncke K (2005) *J Phys Chem B* 109:3053–3064.